Biophysical *Journal*
Article

Biophysical Society

Environmental Calcium Controls Alternate Physical States of the *Caulobacter* Surface Layer

Jonathan Herrmann,[1,2,*] Fatemeh Jabbarpour,[1] Paul G. Bargar,[3] John F. Nomellini,[4] Po-Nan Li,[5] Thomas J. Lane,[2] Thomas M. Weiss,[2] John Smit,[4] Lucy Shapiro,[6,*] and Soichi Wakatsuki[1,2,*]

[1]Department of Structural Biology, Stanford University, Stanford, California; [2]Bioscience Division, SLAC National Accelerator Laboratory, Menlo Park, California; [3]Menlo-Atherton High School, Atherton, California; [4]Department of Microbiology and Immunology, University of British Columbia, Vancouver, British Columbia, Canada; [5]Department of Electrical Engineering and [6]Department of Developmental Biology, Stanford University, Stanford, California

ABSTRACT Surface layers (S-layers) are paracrystalline, proteinaceous structures found in most archaea and many bacteria. Often the outermost cell envelope component, S-layers serve diverse functions including aiding pathogenicity and protecting against predators. We report that the S-layer of *Caulobacter crescentus* exhibits calcium-mediated structural plasticity, switching irreversibly between an amorphous aggregate state and the crystalline state. This finding invalidates the common assumption that S-layers serve only as static wall-like structures. In vitro, the *Caulobacter* S-layer protein, RsaA, enters the aggregate state at physiological temperatures and low divalent calcium ion concentrations. At higher concentrations, calcium ions stabilize monomeric RsaA, which can then transition to the two-dimensional crystalline state. *Caulobacter* requires micromolar concentrations of calcium for normal growth and development. Without an S-layer, *Caulobacter* is even more sensitive to changes in environmental calcium concentration. Therefore, this structurally dynamic S-layer responds to environmental conditions as an ion sensor and protects *Caulobacter* from calcium deficiency stress, a unique mechanism of bacterial adaptation. These findings provide a biochemical and physiological basis for RsaA's calcium-binding behavior, which extends far beyond calcium's commonly accepted role in aiding S-layer biogenesis or oligomerization and demonstrates a connection to cellular fitness.

INTRODUCTION

Surface layers (S-layers) are abundant, proteinaceous components of the cell envelope found in most archaea and a great number of bacteria (1–4). S-layers usually consist of a single protein (40–200 kDa) that oligomerizes into a repeating lattice structure (5). S-layers are the outermost cell envelope component in many bacteria and cover the entire cell surface. As such, S-layers are highly expressed and exceptionally stable as they face variable extracellular conditions (5,6). Indeed, many S-layer proteins lack cysteine residues to prevent redox-mediated misfolding and represent up to 15% of total cellular protein production (4,6–8). These characteristics have made S-layer proteins useful agents for nanopatterning, antigen display, and heterologous protein expression (9,10). In this study, we characterize the in vivo and in vitro behavior of the S-layer protein from *Caulobacter crescentus*.

C. crescentus, a dimorphic bacterium that begins its life cycle as a flagellated swarmer cell before differentiating into a nonmotile stalked cell, displays an S-layer with hexagonal unit cells spaced at a center-to-center distance of ~22 nm (11,12). The *Caulobacter* S-layer consists of a single 98-kDa protein, RsaA (8). The primary sequence of RsaA orchestrates three distinct functions: secretion, anchoring, and two-dimensional (2D) crystallization (Fig. 1). Previously, mutational analysis of RsaA identified 82 residues at the C terminus as responsible for secretion through a type I ABC transporter (13–15). Consistent with this discovery is the presence of six repeat-in-toxin (RTX) motifs in the RsaA sequence, which canonically bind divalent calcium ions to enhance refolding of secreted proteins (8,16). Unsurprisingly, calcium has been shown to specifically mediate 2D crystallization of RsaA in vitro (17). N-terminal deletion/insertion studies determined that the first 225 residues are sufficient for in vivo anchoring to the cell surface (18,19). This function has been attributed to a noncovalent interaction between RsaA and a specific lipopolysaccharide, O-polysaccharide (OPS), found in the outer membrane (20,21). Mutations in genes responsible for production of OPS lead

Submitted February 7, 2017, and accepted for publication April 6, 2017.

*Correspondence: jherrma2@stanford.edu or shapiro@stanford.edu or soichi.wakatsuki@stanford.edu

Editor: Elizabeth Rhoades.

http://dx.doi.org/10.1016/j.bpj.2017.04.003

© 2017 Biophysical Society.

This is an open access article under the CC BY-NC-ND license (http://creativecommons.org/licenses/by-nc-nd/4.0/).

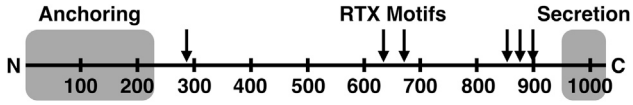

FIGURE 1 Functional components of the RsaA amino acid sequence. The N-terminal 225 residues of RsaA are responsible for anchoring to the cell membrane whereas the C-terminal 82 residues are sufficient for secretion (*gray boxes*). Six RTX motifs (*arrows*) are found in between and are predicted to bind calcium, which might trigger 2D crystallization in vitro.

to an S-layer shedding phenotype, further supporting a role for this interaction in anchoring (22).

Interestingly, mutations in OPS synthesis genes also render *Caulobacter* insensitive to calcium deficiency stress (20,22). *Caulobacter* requires calcium for normal growth, stalk development, and phosphate acquisition (20,23). Whereas most bacteria require only nanomolar concentrations of calcium, minimal and rich *Caulobacter* growth medium contain 500 μM $CaCl_2$ (24,25). The reason *Caulobacter* requires such a high concentration of calcium remains a mystery; however, several proteins predicted to interact with calcium are encoded in the *Caulobacter* genome (26). Among these are genes encoding enzymes dependent on calcium for activity as well as infrastructural proteins such as calcium-specific porins and the S-layer protein, RsaA, characterized extensively in this study (17,26–29). Although prokaryotic calcium signaling is still a nascent field, genomic evidence shows that bacteria contain many calcium-binding proteins involving diverse cellular processes (24). As we will describe, the structural state of the S-layer plays a role in mediating *Caulobacter's* observed calcium sensitivity.

Many S-layer functions arise from their periodic, 2D structure, which produces regularly spaced and sized pores (30,31). These pores have been shown to act as a molecular sieve, protecting the cell from large foreign agents (10,32). The previously determined 2-nm resolution electron cryotomographic reconstruction of the RsaA S-layer indicates pore widths of 2.5–3.5 nm (11). Known functions of RsaA include protection against antimicrobial peptides and *Bdellovibrio exovorus* predation (33–35). Although it is not known whether the charge, geometry, or some other aspect of the S-layer is responsible for these functions, it has been assumed that S-layer proteins generally maintain a single geometry (36,37). Here, we present evidence that *Caulobacter* responds to environmental calcium availability by modulating S-layer crystallinity through an alternate irreversible amorphous aggregate state of RsaA. Under conditions of calcium stress (low calcium levels), RsaA assembles irreversibly into an amorphous aggregate. High levels of calcium stabilize RsaA monomers; these monomers alone convert to the crystalline state. We also found that *Caulobacter* can grow efficiently at low concentrations of calcium, but when the *RsaA* gene is deleted, growth is compromised. Thus, the presence of the amorphous aggregate state protects the cell against exposure to calcium deficiency. We propose a unique function of S-layers in ion sensing, providing, to our knowledge, a new mechanism of bacterial adaptation.

MATERIALS AND METHODS

Strains

Two strains were used in this study. *C. crescentus* CB15N/NA1000, which is referred to as wild-type throughout the text, was used for all protein isolation and microscopy experiments. Strain UJ2602, an RsaA-negative strain of NA1000, was also used for growth curves and was constructed as described in (38). UJ2602 is referred to as *ΔrsaA* throughout the text.

Protein purification

RsaA was purified as reported in Walker et al. (39). Specifically, *C. crescentus* CB15N/NA1000 was grown to stationary phase at 30°C in PYE medium (25), shaking at 200 rpm. The culture was then pelleted by centrifugation and stored at −80°C. Cell pellets were thawed on ice and washed three times with cold 10 mM HEPES buffer pH 7.4. For a dense 500 mL culture, 10 mL of buffer was used per wash. After washing, the pellet was separated into 10 aliquots and 600 μL of 100 mM HEPES buffer pH 2.0 was added to each aliquot. This cell suspension was incubated at 4°C unless otherwise specified for 10–15 min, at which point the suspensions were spun for 5 min at 12,000 rpm. The supernatant was then collected and adjusted to pH 7.0 by the addition of 5 N NaOH. Additionally, 5 mM EDTA was added to remove free divalent cations. The protein solution was then syringe filtered using a 0.22 μm PES syringe filter and injected onto a Highload Superdex 200 16/600 size exclusion column (GE Healthcare Life Sciences, Chicago, IL). During size exclusion chromatography, the running buffer consisted of 50 mM Tris/HCl buffer pH 8.0 with 150 mM NaCl. Monomeric RsaA consistently eluted at ~0.56 column volumes. From 500 mL of dense culture, we consistently purified ~3 mg of monomeric RsaA. Purity was assessed by sodium dodecyl sulfate-polyacrylamide gel electrophoresis (Fig. S1).

Growth experiments

For analysis of soluble and insoluble RsaA in calcium-deficient conditions, a mid-log phase culture grown in M2G medium (25) was harvested by centrifugation and, without washing, resuspended in M2G medium without added $CaCl_2$ (final $CaCl_2$ concentration = 8 μM). The culture was then incubated at 30°C, shaking at 180 rpm with aliquots removed every hour. Soluble RsaA extraction was performed as above and the remaining pellets were solubilized by 8M urea before both samples were analyzed by Western blot using anti-RsaA serum at a dilution of 1:30,000. Immunoblots were visualized by infrared imaging of IRDye 800CW conjugated to goat anti-rabbit secondary antibody (Li-Cor, Lincoln, NE).

For growth curve analysis of wild-type and *ΔrsaA Caulobacter* strains, 1 μL of mid-log phase cultures (OD_{600nm} = 0.5) of wild-type and *ΔrsaA* strains grown in M2G medium (500 μM $CaCl_2$) were inoculated into 150 μL M2G medium containing $CaCl_2$ concentrations between 100 and 400 μM in a 96-well transparent plate. OD_{600nm} was measured every 10 min for 30 h using an Epoch 2 Microplate Spectrometer (BioTek, Winooski, VT).

ThermoFluor assay

Using monomeric protein with a concentration between 0.2 and 1 mg/mL, 45 μL was mixed with 5 μL of 10× ion solution (or water) as well as 0.5 μL of 10,000× SYPRO Orange Protein Gel Stain (excitation/emission

wavelength, $\lambda = 490/590$ nm; Thermo Fisher Scientific, Waltham, MA). Temperature was increased at a rate of 1°C per minute from 4 to 100°C and fluorescence was measured every minute with a qPCR thermocycler in FRET mode (Bio-Rad, Hercules, CA). Aggregation temperature was determined by locating the global minimum of the second derivative of the raw data. Binding data were fit to a single-site binding model using the software Prism (GraphPad, La Jolla, CA).

Small angle x-ray scattering/diffraction

Small angle x-ray scattering (SAXS) experiments were performed at the bio-SAXS beamline BL4-2 (40) at the Stanford Synchrotron Radiation Lightsource. Data were collected using a model No. MX225-HE charge-coupled device detector (Rayonix, Evanston, IL) with a 3.5 m sample-to-detector distance and beam energy of 11 keV (wavelength, $\lambda = 1.127$ Å). SAXS data were measured in the range of $0.0033\ \text{Å}^{-1} \leq q \leq 0.27\ \text{Å}^{-1}$ ($q = 4\pi\sin(\theta)/\lambda$, with θ being the scattering angle). The q scale was calibrated with silver behenate powder and the data were plotted on an absolute scale using the scattering intensity of pure water. The RsaA solution aliquots were injected directly into a temperature-controlled flow cell. The SAXS data were taken in a series of 12 1-s exposures. These images were then analyzed for possible effects of radiation damage, normalized according to the transmitted intensity, and averaged using the program SasTool (http://ssrl.slac.stanford.edu/~saxs/analysis/sastool.htm). The scaled and averaged buffer curve was then subtracted from the averaged protein curve. For powder diffraction analysis, peaks were identified by hand and indexed using the software JADE (Jade Software, Jacksonville, FL).

Electron microscopy

A quantity of 3 μL of protein (1 mg/mL) or cell sample ($OD_{600\text{nm}} = 0.3$) was deposited onto the surface of glow-discharged 300 mesh carbon-coated copper transmission electron microscopy (TEM) grids (Cat. No. CF300-Cu; Electron Microscopy Sciences, Hatfield, PA) and allowed to sit for 1 min. The sample was then blotted and 3 μL of 1% uranyl acetate for soluble protein samples or 2% ammonium molybdate for cell or crystal samples was added. After 30 s to 1 min of incubation, the grid was blotted dry and transferred to a Tecnai TF20 transmission electron microscope (FEI, Hillsboro, OR) equipped with a K2 direct electron detector (Gatan, Pleasanton, CA). Images were collected for 6 s in dose fractionation mode (200 ms/image) at 1.5–7 μm defocus. Motion correction was performed using Gatan's Digital Micrograph software. Calculation of 2D image autocorrelation was performed using the software MATLAB (The MathWorks, Natick, MA).

Circular dichroism spectroscopy

Circular dichroism (CD) measurements were performed using a model No. 202-01 Circular Dichroism Spectrometer (Aviv Biomedical, Lakewood, NJ). Far-UV spectra (200–250 nm) were recorded in a 1 mm path-length cell with an exposure time of 1 s/nm. The sample cell was maintained at 15°C and five scans were collected and averaged for each sample. Monomeric, crystallized, and aggregated RsaA samples were prepared separately in PBS (Sigma-Aldrich, St. Louis, MO) and brought to a final concentration of 1.8 μM. A buffer spectrum was subtracted from all sample spectra before plotting.

RESULTS AND DISCUSSION

Calcium depletion decreases s-layer long-range crystallographic order in vivo

Recent technological advances have allowed direct visualization of S-layers at high resolution through cryo-electron tomography (41,42). When *Caulobacter* was examined in this way, Amat et al. (42) found that its S-layer is not entirely crystalline; rather, the surface was marked by local, short-range crystal lattices with many periodicities. Because in vitro RsaA crystallization is mediated by calcium (17), we sought to determine whether in vivo *Caulobacter* modulates its S-layer crystallinity based on calcium availability. Using negative-stain TEM, we observed the S-layer of *Caulobacter* with and without exogenous calcium. Visualizing whole *Caulobacter* cells by negative-stain TEM is generally difficult due to overstaining. However, by scanning the sample grid one can find naturally lysed cells (1–5% of total cells), which take up less stain and allow for the direct observation of the S-layer using 2% ammonium molybdate (43).

Cells incubated in media for 30 min with or without calcium both exhibit an S-layer that can be observed along the entire edge of the cell, indicating that there are likely no significant gaps in S-layer coverage (Fig. 2, *A* and *B*). Therefore, within the first 30 min of calcium deprivation, the *Caulobacter* S-layer was not shed as was seen previously in calcium-insensitive mutants (20). On the main body of the cells, S-layer unit cells were only visible in areas where the cell was completely empty. Qualitative differences in S-layer crystallinity can be observed between the two differently treated cells (Fig. 2, *A* and *B*). In a cell grown in the presence of 500 μM $CaCl_2$ (Fig. 2 *A*), we see several highly ordered S-layer regions as evidenced by 2D autocorrelation

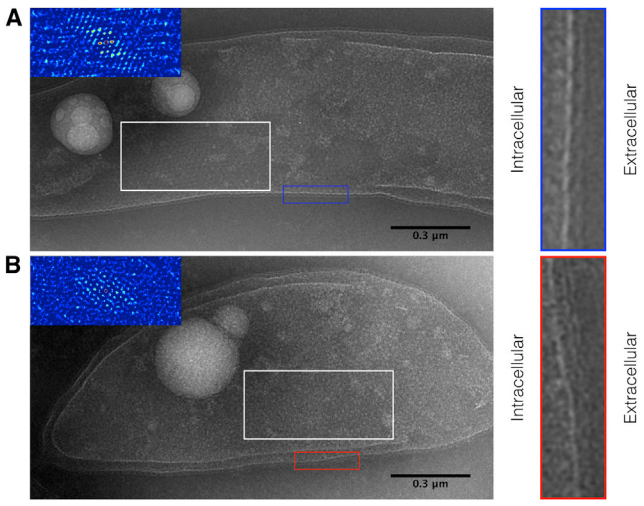

FIGURE 2 Physiological evidence for multiple RsaA structural states. (*A* and *B*) TEMs of naturally lysed *Caulobacter* cells were incubated for 30 min in minimal medium with 500 μM $CaCl_2$ (*A*) or minimal medium without calcium (*B*). Two regions with visible S-layer unit cells are marked by shaded boxes. Autocorrelation of the shaded boxed regions (*insets*) indicate higher long-range order in the cell incubated with calcium. The easily observable cell edges shown at the right in blue (*A*) or red (*B*) boxes indicate that the S-layer was not shed during the 30 min incubation time with or without calcium. Cells were stained with 2% ammonium molybdate. Scale bars represent 0.3 μm. To see this figure in color, go online.

exhibiting long-range hexagonal symmetry. For a cell incubated in calcium-deficient media for 30 min, regions where the S-layer is visible exhibit less long-range order as evaluated by 2D autocorrelation of an identically sized region (Fig. 2 *B*). Therefore, removal of exogenous calcium for 30 min causes a decrease in S-layer crystallographic long-range order as confirmed by image autocorrelation.

RsaA undergoes temperature-dependent aggregation in vitro

To characterize the noncrystalline form of the *Caulobacter* S-layer, we isolated and purified the S-layer protein, RsaA, using a previously reported isolation protocol (39). This protocol consists of treating *Caulobacter* with dilute acid, which disrupts calcium and OPS binding. Calcium binding is responsible for crystallization, while OPS binding anchors RsaA to the outer membrane. In this way, RsaA is solubilized and can be further purified by size exclusion chromatography (Fig. S1). When RsaA was purified at 4°C and run on a Superdex 200 gel filtration column (GE Healthcare Life Sciences), a peak appeared after an elution of 0.56 column volumes (Fig. 3 *A*). When RsaA extract was incubated at room temperature before size exclusion chromatography, a second peak appeared in the elution profile (Fig. 3 *A*). This larger peak eluted at the expected void volume of the size exclusion column, indicating an average molecular weight above 600 kDa.

The material in each of the two peaks was isolated separately, concentrated, and observed by SAXS (Fig. 3 *B*). The Kratky plot and pair-distance distribution function $P(r)$ of the lower-molecular-weight sample indicate a slightly flexible protein with multiple domains (Fig. 3, *C* and *D*) and the resulting Guinier analysis yielded a radius of gyration of 58.0 Å with a molecular mass of 86 kDa—close to the theoretically expected value of 98 kDa for a monomeric species (Fig. 3 *E*). The SAXS data from the high-molecular-weight sample is not linear in the Guinier regime, implying that the sample may consist of large, heterogeneous particles (Fig. 3 *F*). Indeed, negative-stain TEM of the low molecular

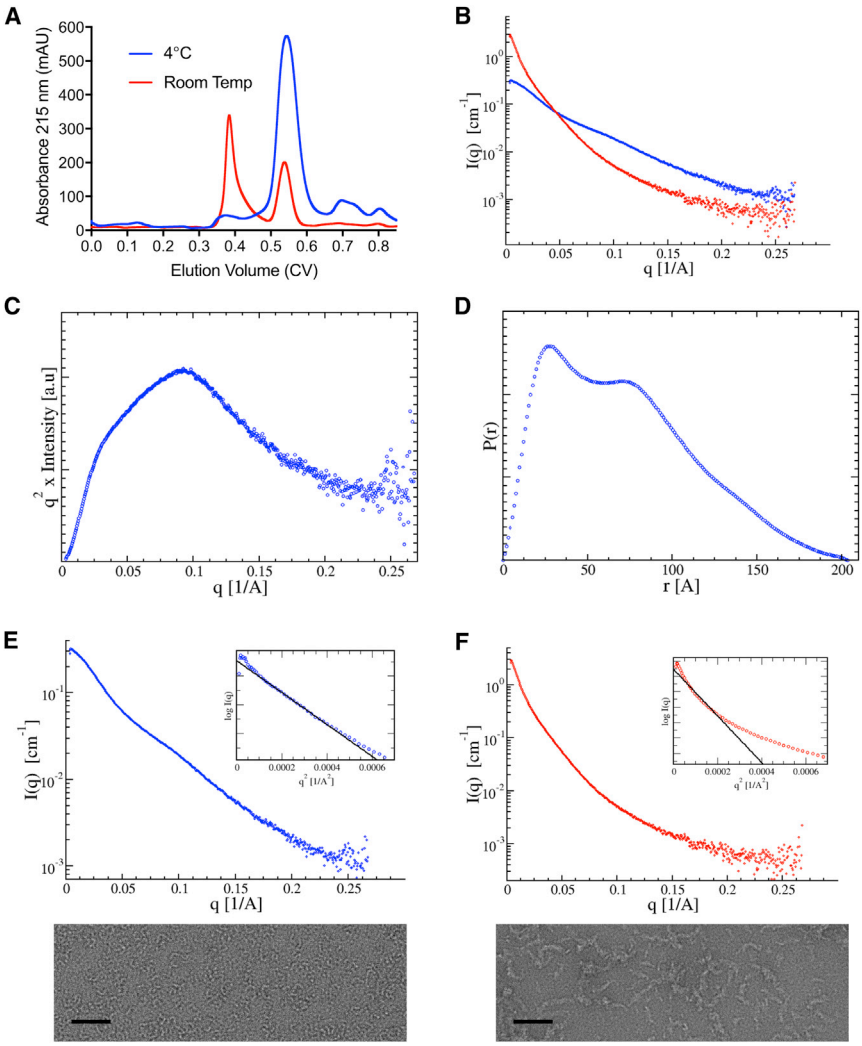

FIGURE 3 Characterization of RsaA's two soluble states in vitro. (*A*) Shown here are size exclusion chromatograms of RsaA purified at 4°C (*blue*) and room temperature (*red*). See also Fig. S1. (*B*) Shown here is an overlay of SAXS data of 5 mg/mL RsaA at 4°C (*blue*) and 4 mg/mL RsaA at 30°C. Higher scattering at low q indicates a larger particle size in the heated sample. (*C*) Given here is a Kratky plot of 5 mg/mL RsaA at 4°C. The data exhibit a pronounced peak with a shoulder consistent with a folded multidomain protein. As the data do not fully return to the baseline at high q values, the domains are likely to be connected by somewhat flexible linkers. (*D*) The pair-distance distribution function $P(r)$ of RsaA at 4°C exhibits a double peak consistent with a multidomain protein. (*E*) SAXS data of 5 mg/mL RsaA at 4°C with Guinier analysis (*inset*) indicates a monomeric species (*top*). TEM of RsaA at 4°C stained with 1% uranyl acetate confirms a monomeric sample (*bottom*). (*F*) SAXS data of 4 mg/mL RsaA at 30°C with Guinier analysis (*inset*) indicates a highly aggregated sample (*top*). TEM of RsaA at 30°C stained with 1% uranyl acetate confirms a heterogeneous aggregated sample. Scale bars represent 50 nm. To see this figure in color, go online.

weight sample showed homogeneous particles with a size consistent with monomers whereas the larger-molecular-weight sample showed a heterogeneous distribution of particle sizes much larger than a monomeric species (Fig. 3, *E* and *F*). Therefore, RsaA forms an amorphous, soluble aggregate when heated to room temperature.

Monomeric RsaA can crystallize in vitro whereas aggregated RsaA cannot

Previously, RsaA purified by acid extraction was shown to crystallize in vitro in the presence of 1 mM $CaCl_2$ (17). However, it is unclear whether the purified protein solution used consisted of monomeric or aggregated RsaA. We evaluated the reversibility of RsaA aggregation by purifying monomeric RsaA at 4°C and subsequently incubating the sample at 32°C for 15 min. The sample was then cooled to 4°C and run on a size exclusion column. A monomeric peak no longer appeared, but was replaced by a peak at the void volume of the column (Fig. 4 *A*), indicating a complete and stable conversion of monomeric RsaA to a higher-order aggregated state. Similarly, when 1 mM $CaCl_2$ was added to aggregated RsaA at 32°C, the sample remained aggregated when run on a size exclusion column at 4°C (Fig. 4 *A*). This experiment was performed at low RsaA concentration, 0.25 mg/mL, so that calcium addition would not cause crystallization, a process that would appear the same as aggregation on a size exclusion column. These data indicate that both cooling and calcium addition are unable to reverse RsaA aggregation. Thus, the aggregated state is a dead-end in the described cases.

We therefore sought to determine whether both monomeric and aggregated RsaA are competent for 2D crystallization. Given the insensitivity of RsaA to calcium in the aggregated state, it is reasonable to predict that only monomeric RsaA can crystallize. When 10 mM $CaCl_2$ was added to a sample of 7.5 mg/mL monomeric RsaA at 4°C, the sample became turbid within seconds (Fig. 4 *B*). However, when 10 mM $CaCl_2$ was added to an aggregated sample at the same concentration and temperature, the solution remained clear (Fig. 4 *B*). When the turbid sample was imaged by negative-stain electron microscopy, clear 2D crystals were observed (Fig. 4 *C*). The Fourier transform of the image indicates the expected *p6* symmetry (Fig. 4 *C*, *inset*).

RsaA crystallization was further observed by small angle x-ray scattering/diffraction. Five concentrations of RsaA with 10 mM $CaCl_2$ were heated to 30°C and exposed to 11 keV x-rays (Fig. 4 *D*). The resulting SAXS profiles indicated concentration-dependent crystallization as the two lowest concentrations (0.5 and 1.0 mg/mL) exhibited solution-state scattering whereas higher concentrations (2.0, 4.0, and 8.0 mg/mL) produced powder diffraction (Fig. 4 *D*, *inset*). The low concentration scattering profiles show traces of larger particles as evidenced by nonlinear signal in the Guinier regime; however, these profiles largely resemble those of monomeric RsaA and differ greatly from high-temperature samples lacking calcium (i.e., aggregated samples) (Fig. S2). Therefore, in vitro, monomeric RsaA is the dominant species in samples that crystallize.

To confirm that the diffraction we observed in high concentration samples was that of 2D S-layer crystals, we indexed the seven lowest-angle peaks observed using the JADE software package (Fig. 4 *D*). Indexing in a hexagonal lattice yielded unit cell dimensions of $a = b = 22.2$ nm, which match our electron micrographs (Fig. 4 *C*) as well as previous measurements (11,42). Predicted peak locations

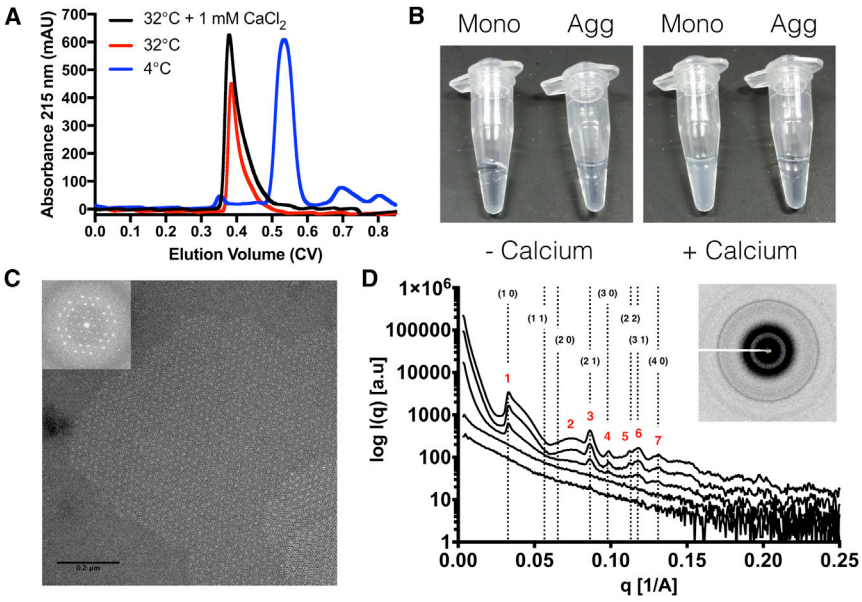

FIGURE 4 Reversibility and crystallizability of monomeric and aggregated RsaA in vitro. (*A*) Shown here are size exclusion chromatograms of monomeric RsaA kept at 4°C (*blue*), heated to 32°C for 10 min, then cooled to 4°C (*red*) and heated to 32°C for 10 min before the addition of 1 mM $CaCl_2$, and then cooled to 4°C (*black*). (*B*) Shown here is a precipitation test of monomeric and aggregated RsaA at 7.5 mg/mL. Upon the addition of 10 mM $CaCl_2$, only monomeric RsaA precipitates. (*C*) TEM of 8 mg/mL monomeric RsaA with 10 mM $CaCl_2$ stained with 2% ammonium molybdate reveals 2D crystallization. *P6* symmetry can be seen in the Fourier transform of the image (*inset*). Scale bars represent 0.2 μm (*D*) SAXS/D of (from *bottom* to *top*) 0.5, 1, 2, 4, and 8 mg/mL RsaA with 10 mM $CaCl_2$ at 30°C. Peaks used for indexing are denoted by red numbers. Vertical dotted lines indicate predicted peaks with corresponding Miller indices shown assuming a hexagonal lattice with unit cell parameters $a = b = 22.2$ nm. Powder diffraction image of the 8 mg/mL sample is also shown (*inset*). See also Fig. S2. To see this figure in color, go online.

for the previously described unit cell parameters agree well with our data for the observed peaks 1 and 3–7. The two peaks with Miller indices of (11) and (20) are, however, missing from our data, although they appear near peak 2, which is unusually broad. This may reflect the particular form factor of this 2D crystal, as Fourier transforms of crystals observed by EM exhibit the same ring pattern (data not shown). On the basis of microscopy, precipitation, and x-ray scattering, we reason that the observed diffraction patterns arise from the formation of 2D crystals of RsaA from a monomeric protein pool upon the addition of calcium.

Calcium stabilizes monomeric RsaA and prevents aggregate formation in vitro

Because calcium appeared to decrease aggregation at 30°C in the previous SAXS experiment, we employed the ThermoFluor assay to assess the aggregation temperature of in vitro RsaA under various conditions. In the absence of divalent cations, RsaA's aggregation temperature is 28°C (Fig. 5, *A* and *B*)—at the low end of *Caulobacter's* typical laboratory growth condition of 28–30°C. The aggregation temperature did not appear to shift significantly when varying the concentration of RsaA from 2.5 to 10 μM (Fig. 5, *A* and *B*). Adding various chloride salts, except for calcium chloride, had no effect on aggregation temperature when compared to a sample containing 5 mM EDTA (Fig. 5, *C* and *D*). Monomeric RsaA was significantly stabilized by 1 mM $CaCl_2$, as evidenced by a shift in the aggregation temperature from 28 to 41°C (Fig. 5, *C* and *D*). Using this temperature shift as a proxy for calcium binding to monomeric RsaA, aggregation temperatures were determined for various $CaCl_2$ concentrations. The resulting data were fit to a single-site binding model to find that calcium maximally confers 13.2 $\pm$ 1.1°C of RsaA monomer stability, preventing the formation of aggregates at 28°C. The binding affinity for the interaction between monomeric RsaA and calcium is 172 $\pm$ 56 μM (Fig. 5, *E* and *F*). Thus, divalent calcium ions stabilize monomeric RsaA by preventing amorphous aggregation at low temperature.

In vitro, aggregated RsaA is partially unfolded

To provide structural insight into the observed aggregation behavior of RsaA, we evaluated the secondary structure composition of all three states in vitro by far-UV CD spectroscopy. Samples of monomeric, crystallized (10 mM $CaCl_2$), and aggregated RsaA were prepared and brought to identical temperature and concentration, 15°C and 1.8 μM, respectively. Monomeric and crystallized RsaA exhibited almost identical CD spectra, displaying a large negative band between 210 and 220 nm (Fig. 6). This indicates RsaA contains a mixture of α-helical and β-stranded secondary structures. Notably, aggregated RsaA yielded a CD spectrum with a significantly shallower band, indicating

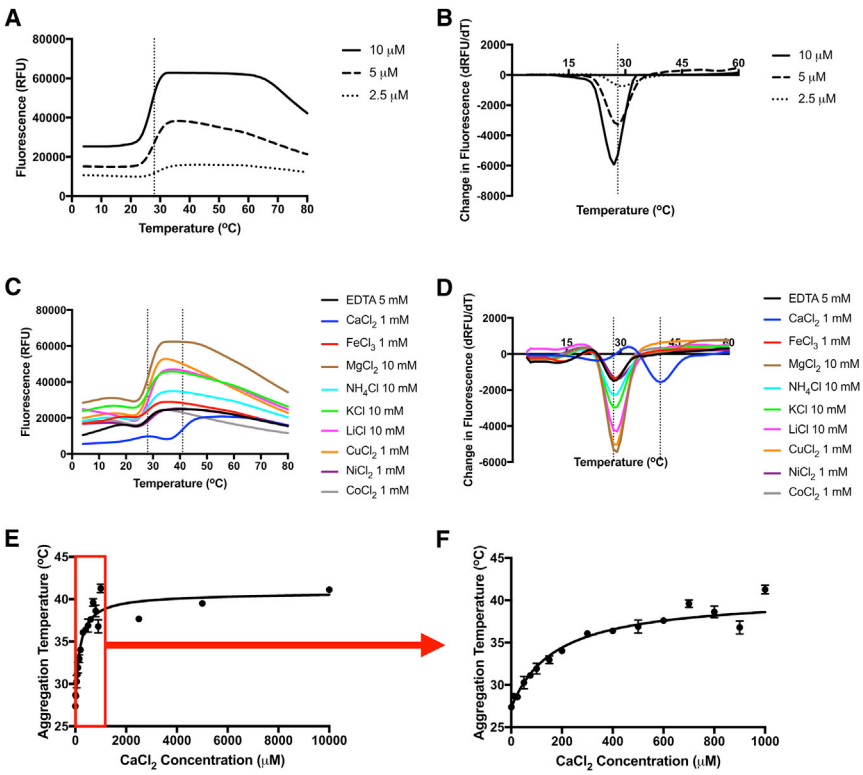

FIGURE 5 RsaA preferentially binds calcium to stabilize the monomeric species in vitro. Shown here are ThermoFluor assay melting curves (*A*) and their second derivatives (*B*) of 10 μM (*solid*), 5 μM (*dashed*), and 2.5 μM (*dotted*) RsaA. Vertical dotted lines denote 28°C. Given here are melting curves (*C*) and their second derivatives (*D*) of 8 μM RsaA with various chloride salts. Vertical dotted lines denote 28°C and 41°C. Shown also are full view (*E*) and zoom (*F*) of RsaA aggregation temperature shifts plotted against $CaCl_2$ concentration. The data were fit to a single-site binding model. Maximum stabilization is 13.2 $\pm$ 1.1°C, and the calculated K_d = 172 $\pm$ 56 μM with an R^2 of 0.94 for n = 3. Data are represented as mean $\pm$ standard error. To see this figure in color, go online.

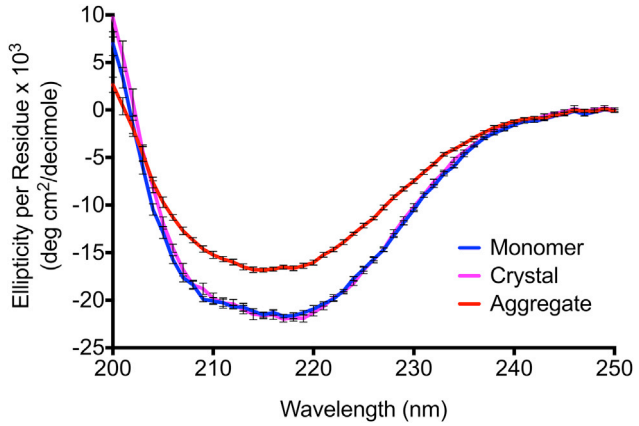

FIGURE 6 Aggregated RsaA is less folded than the monomeric or crystallized forms in vitro. Shown here are far-UV circular dichroism spectra of monomeric (*blue*), crystallized (*magenta*), and aggregated (*red*) RsaA at 1.8 μM and 15°C. Each spectrum is an average of five scans, with standard error measurements shown. The shallower band of the aggregated sample indicates a decrease in folded secondary structure. To see this figure in color, go online.

partial loss of folded secondary structure (Fig. 6). Therefore, the aggregated state of RsaA is partially unfolded.

Upon calcium removal in vivo, newly secreted RsaA aggregates whereas crystallized RsaA remains folded

Because the structural state of RsaA appears to be mediated by calcium, we sought to determine the mechanism by which calcium depletion disrupts long-range S-layer order as seen in Fig. 2. To do this, we isolated RsaA as either amorphous aggregate or monomeric/crystallized fractions after calcium depletion. We expected that cells incubated in culture medium lacking calcium would produce an increase in aggregated RsaA using either newly secreted RsaA or already crystalline RsaA as the source. Whereas we have shown that monomeric RsaA can transition to the aggregate state, crystallized RsaA can also undergo this transition. SAXS of RsaA crystals at 30°C produces powder diffraction; but at 55°C, we observed a SAXS profile consistent with an amorphous aggregate indicating that, at high temperatures, crystalline RsaA can become aggregated (Fig. S3).

Cells grown in calcium-replete minimal medium were transferred to media lacking calcium (final concentration = 8 μM) and grown for another 6 h. Monomeric RsaA was isolated by acid extraction as described above, whereas remaining aggregated RsaA was collected by solubilizing the leftover pellets from the acid extraction protocol with 8M urea. Because our extracted RsaA samples were almost exclusively monomeric when run on a size exclusion column (Fig. 3 *A*), we reasoned that when extracting RsaA from the cell surface with 0.1M HEPES buffer pH 2.0, only crystallized or monomeric RsaA comes free, and that the acid extraction protocol does not prevent or reverse RsaA aggregation (Fig. S4). The relative amount of RsaA in each fraction was measured by Western blot, which showed that aggregated RsaA increased by more than twofold over the 6-h calcium depletion, while soluble RsaA levels remained fixed. (Fig. 7 *A*). Therefore, calcium depletion in culture medium causes newly secreted RsaA to aggregate, whereas previously crystalline RsaA remains folded.

RsaA is required to recover from calcium deficiency stress in vivo

Caulobacter cultures typically require 500 μM $CaCl_2$ for optimal growth. To determine if RsaA contributes to this requirement for exogenous $CaCl_2$, we measured growth curves of wild-type and *ΔrsaA Caulobacter* in minimal medium containing between 103 and 403 μM $CaCl_2$ (Fig. 7, *B* and *C*). Both wild-type and *ΔrsaA* cells grew in M2G medium containing 403 μM $CaCl_2$, although the *ΔrsaA* strain exhibited a doubling time twice that of wild-type (7 vs. 3.5 h). Wild-type doubling times are usually closer to 2 h,

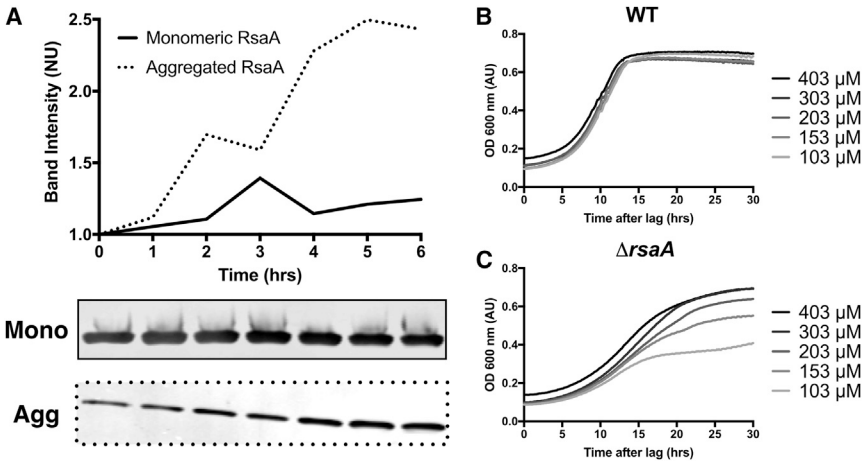

FIGURE 7 RsaA is required for normal growth at low calcium concentrations. (*A*) Shown here is Western blot analysis of monomeric (*solid*) and aggregated (*dotted*) RsaA under calcium deprivation conditions. Monomeric RsaA was collected via dilute acid treatment, whereas aggregated RsaA was solubilized in 8M urea before gel electrophoresis. Band intensities were normalized to time point zero. See also Figs. S3 and S4. (*B* and *C*) Shown here are growth curves of wild-type (*B*) and *ΔrsaA* (*C*) *Caulobacter* in M2G growth medium with calcium concentrations ranging from 403 to 103 μM (*solid to shaded*, respectively). Growth curves were run in triplicate, but representative curves are shown.

but limitations in aeration of low-volume cultures in 96-well plates most likely contributed to the observed slower growth rates. Wild-type *Caulobacter* was insensitive to calcium concentrations as low as 103 μM (Fig. 7 *B*); however, the *ΔrsaA* strain demonstrated a marked decrease in growth rate and maximum culture density in media containing <203 μM $CaCl_2$ (Fig. 7 *C*).

CONCLUSIONS

In this report, we present evidence for a structurally dynamic S-layer in *C. crescentus*. We show that the S-layer protein, RsaA, can exist in two soluble states: monomeric and aggregated (Fig. 8). In vitro, RsaA amorphous aggregation occurs at 28°C in the presence of low levels of calcium, whereas at this temperature monomeric RsaA is stabilized significantly by the addition of calcium leading to its crystallization. The equilibrium calcium concentration of this stabilizing interaction is 172 μM—just less than half the concentration of exogenous calcium in typical *Caulobacter* growth media. Once aggregated, RsaA cannot return to the monomeric state either by cooling or by the addition of calcium. Interestingly, only monomeric RsaA can form 2D crystals, the canonical state of S-layer proteins in vivo (Fig. 8).

Much of S-layer research over the past 30 years has focused on the biogenesis and inherent paracrystallinity of oligomerized S-layer proteins (4–6,44). Diverse functions over many archaeal and bacterial families are attributable to S-layer crystallinity. These functions include protection, protein scaffolding, and shape determination (1–3,5,45). The process of 2D crystallization of several S-layer proteins is well studied; these studies show that crystallization is often mediated by divalent cations, most commonly calcium (17,30,46–50). A recent crystal structure of the bacterial S-layer protein from *Geobacillus stearothermophilus*, SbsB, showed that calcium mediates both inter- and intramolecular interactions in the process of 2D crystallization

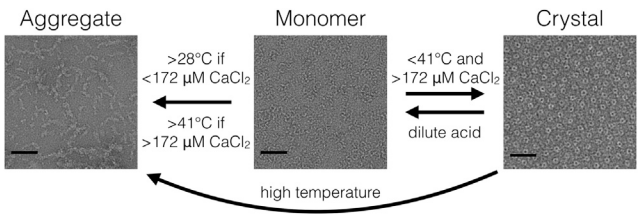

FIGURE 8 Model of the structural states of RsaA. Monomeric RsaA proceeds to the aggregated state at 28°C at low calcium levels. With calcium (K_d = 172 μM), the RsaA protein is stabilized (aggregation occurs at 41°C) and can proceed to the crystallized state if protein concentration is high enough. Once crystallized, RsaA can be returned to the monomeric state by treatment with dilute acid or to the aggregated state by heating. Simple calcium removal does not appear to cause crystalline RsaA to transition to the aggregated state. Aggregated RsaA cannot return to the monomeric state and cannot crystallize. Therefore, aggregated RsaA is a dead-end state for the *Caulobacter* S-layer. Scale bars represent 50 nm.

(30). In the case of RsaA from *Caulobacter*, we observed that calcium also serves to stabilize the monomeric species, thereby facilitating 2D crystallization.

A stable noncrystalline state for an S-layer protein has never been characterized; however, evidence pointed toward its existence. An electron cryo-tomogram of *Caulobacter's* S-layer in situ indicated that RsaA is not entirely crystalline (42). Indeed, the authors showed that there are S-layer regions of the surface that are poorly ordered, with less than half the cell covered in a crystalline S-layer in their presented images (42). While some organisms can modulate S-layer structure through differential expression of S-layer genes, no physiological structural transitions other than crystallization have been characterized in S-layer proteins (51).

The molecular mechanism for RsaA's structural plasticity is currently unknown, but RsaA's calcium-binding RTX motifs (Fig. 1) suggest an explanation. RTX motifs are common calcium-binding sequences consisting of tandem β-strand repeats (52). Divalent calcium binds the loops connecting these β-strands through backbone interactions, thereby stabilizing the fold itself (52). Our circular dichroism measurements showed that RsaA is partially unfolded in the aggregated state, further supporting the idea that calcium directly mediates the structural state of RsaA through the unfolding or stabilization of RTX motif β-strands (Fig. 6).

Although domain assignments cannot be made from RsaA's primary sequence, our SAXS measurements indicate a multidomain protein (Fig. 3, *C* and *D*). If RTX motifs are located at domain interfaces, calcium absence could prevent folding between domains and render the structure more flexible and therefore more prone to nonspecific intermolecular interactions and amorphous aggregation (53). This potential mechanism also suggests an explanation for RsaA's 2D crystallization. Although we know that 2D crystallization is mediated by calcium, deleting the N-terminal 222 residues leads to hexameric RsaA that cannot form 2D sheets in vitro (54). These N-terminal residues are located at the *p3* center of the hexagonal crystal lattice, but do not contain a known calcium-binding motif (42), implying that folding of allosteric calcium-binding domains is responsible for correct positioning of the N-terminus for extended oligomerization. High-resolution structural information of full-length RsaA would undoubtedly support or invalidate these hypotheses.

RsaA's calcium-mediated structural switch is reflected in *Caulobacter* physiology. We found by electron microscopy that the S-layer becomes qualitatively less crystalline within 30 min of calcium removal at 30°C, in accord with previously published tomograms that show regions of noncrystallinity (42). Indeed, Western blots of RsaA from calcium-depleted cultures over 6 h show a significant increase in aggregated RsaA. However, Western blots also showed a relatively constant amount of monomeric/crystalline RsaA despite calcium removal for 6 h (Fig. 7 *A*).

Although we know it is possible for crystalline RsaA to transition to the aggregated state at very high temperatures (Fig. S3), we hypothesize that simple removal of calcium is insufficient to destabilize the crystalline form. This would suggest that when environmental calcium falls below 172 μM, previously crystallized RsaA on the cell surface remains crystalline. However, newly secreted RsaA monomers inserted into the existing S-layer will lack sufficient divalent calcium ions to fold properly and will disrupt the existing crystal lattice.

Caulobacter requires micromolar concentrations of calcium for normal growth, stalk development, and phosphate acquisition (20,23). *Caulobacter* mutants that can survive in low calcium concentrations have been isolated and were shown to shed their S-layer (20). These mutants all had defects in O-polysaccharide (OPS) biosynthesis machinery, which removed the outer membrane anchor of RsaA (19,21). Based on the fact that disrupting OPS synthesis adapts *Caulobacter* to low calcium conditions, Walker et al. (20) hypothesized that OPS is toxic to *Caulobacter* in the absence of divalent calcium ions. One possible mechanism for this predicted toxicity is that OPS is charge imbalanced without calcium, which could cause defects in the physical properties of the outer membrane and arrest growth.

Therefore, a possible explanation based on previous work is that the S-layer relieves calcium-dependent toxicity of the underlying OPS. Our growth curves may provide insight into this potential mechanism (Fig. 7, *B* and *C*). Two phenotypes result from the deletion of the gene encoding RsaA. First, doubling time is twice as long in *ΔrsaA* (7 h) compared to wild-type (3.5 h) at all calcium concentrations. Second, wild-type *Caulobacter* grows normally at $CaCl_2$ concentrations as low as 103 μM, but *ΔrsaA* cells reach stationary phase significantly earlier at $CaCl_2$ concentrations below 203 μM. To explain the first phenotype in the context of OPS toxicity, we reason that calcium alone is sufficient to relieve toxicity, albeit with a cost in growth rate. The calcium-dependent culture density defect of *ΔrsaA* occurs at 203 μM, similar to the 172 μM binding constant between calcium and monomeric RsaA (Figs. 5 *E* and 7 *C*). It is possible that an aggregated S-layer is better able to neutralize toxic OPS at low calcium concentrations than a crystalline S-layer, although the mechanism of this potential interaction remains unknown.

Overall, these growth curves indicate that the presence of the S-layer gene, *rsaA*, imparts resistance to calcium deficiency and implicates RsaA and its ability to form amorphous aggregates as a central component in *Caulobacter's* calcium deficiency stress response. The cumulative results of our in vitro and in vivo experiments suggest that RsaA aggregation occurs at the point at which calcium deficiency begins to affect cell fitness. Our identification of a third, aggregated state of RsaA challenges the view that S-layers are functionally limited by their static nature, suggesting, instead that the RsaA S-layer displays dynamic, varied structures with apparent distinct biological functions.

S-layers are surprisingly diverse, exhibiting variable geometry, length, domain organization, and ligand sensitivity (55). However, S-layers are distinctly microbial; there is no known structural or functional proteinaceous homolog in eukaryotic cells (55). Some common microbial pathogens such as *Clostridium difficile*, *Bacillus anthracis*, *Aeromonas salmonicida*, *Aeromonas hydrophila*, and *Paenibacillus larvae* display S-layers (56–60). In this study, we have shown that S-layers can be dynamic entities whose structural state may affect viability under certain conditions. Whereas approaching S-layer research through the lens of structural plasticity promises insights into S-layer biological functions, S-layers have additionally long been valued for their potential as easily manipulated and customizable nanomaterials (9,10). S-layers are currently used in a broad variety of biotechnological capacities including antigen display, nanopatterning, and drug delivery (36,37,61). The crystallinity of S-layers is vitally important to their use in these biotechnological applications. Further characterizing the conditions that allow us to predictively and consistently modulate S-layer structure will accelerate their industrial development and expand possible applications for these distinctive macromolecular structures.

SUPPORTING MATERIAL

Four figures are available at http://www.biophysj.org/biophysj/supplemental/S0006-3495(17)30390-9.

AUTHOR CONTRIBUTIONS

Conceptualization: J.H., J.S., L.S., and S.W. Investigation: J.H., F.J., and P.B. Formal analysis: J.H., P.L., T.L., and T.W. Resources: J.N., J.S., and T.W. Writing—original draft: J.H., T.W., and L.S. Writing—review and editing: J.H., L.S., and S.W. Supervision and funding acquisition: J.S., L.S., and S.W.

ACKNOWLEDGMENTS

Part of this work was performed at the Stanford ChEM-H Macromolecular Structure Knowledge Center and the Stanford Department of Structural Biology Electron Microscopy Center. The authors thank Dong-Hua Chen, Marc Deller, and Ellie Norby for technical support and Thomas Mann and Keren Lasker for a critical reading of the manuscript.

This work was supported by the Department of Energy, Laboratory Directed Research and Development (co-PI: John Bargar), under contract No. DE-AC02-76SF00515. This material is based upon work supported by the U.S. Department of Energy, Office of Science, Office of Biological and Environmental Research, Mesoscale to Molecules: Bioimaging Science Program. J.H. was supported by the National Science Foundation Graduate Research Fellowship Program (NSF-GRFP) as well as the Department of Energy Office of Science Graduate Student Research Program (DOE-SCGSR). J.S. was supported by a grant from the Natural Sciences and Engineering Research Council of Canada. L.S. was supported by NIH-NIGMS

R35118072A. Use of the Stanford Synchrotron Radiation Lightsource, SLAC National Accelerator Laboratory, is supported by the U.S. Department of Energy, Office of Science, Office of Basic Energy Sciences under contract No. DE-AC02-76SF00515. The Stanford Synchrotron Radiation Lightsource Structural Molecular Biology Program is supported by the DOE Office of Biological and Environmental Research, and by the National Institutes of Health, National Institute of General Medical Sciences (including grant No. P41GM103393).

REFERENCES

1. Albers, S.-V., and B. H. Meyer. 2011. The archaeal cell envelope. *Nat. Rev. Microbiol.* 9:414–426.
2. Sleytr, U. B., and M. Sára. 1997. Bacterial and archaeal S-layer proteins: structure-function relationships and their biotechnological applications. *Trends Biotechnol.* 15:20–26.
3. Gerbino, E., P. Carasi, …, A. Gómez-Zavaglia. 2015. Role of S-layer proteins in bacteria. *World J. Microbiol. Biotechnol.* 31:1877–1887.
4. Sleytr, U. B., P. Messner, …, M. Sára. 1993. Crystalline bacterial cell surface layers. *Mol. Microbiol.* 10:911–916.
5. Fagan, R. P., and N. F. Fairweather. 2014. Biogenesis and functions of bacterial S-layers. *Nat. Rev. Microbiol.* 12:211–222.
6. Engelhardt, H., and J. Peters. 1998. Structural research on surface layers: a focus on stability, surface layer homology domains, and surface layer-cell wall interactions. *J. Struct. Biol.* 124:276–302.
7. Lau, J. H. Y., J. F. Nomellini, and J. Smit. 2010. Analysis of high-level S-layer protein secretion in *Caulobacter crescentus*. *Can. J. Microbiol.* 56:501–514.
8. Gilchrist, A., J. A. Fisher, and J. Smit. 1992. Nucleotide sequence analysis of the gene encoding the *Caulobacter crescentus* paracrystalline surface layer protein. *Can. J. Microbiol.* 38:193–202.
9. Sleytr, U. B., B. Schuster, …, D. Pum. 2014. S-layers: principles and applications. *FEMS Microbiol. Rev.* 38:823–864.
10. Sleytr, U. B., B. Schuster, …, N. Ilk. 2011. Nanobiotechnology with S-layer proteins as building blocks. *In* Progress in Molecular Biology and Translational Science, *Vol. 103*. H. Stefan, editor.. Academic Press, Amsterdam, the Netherlands, pp. 277–352.
11. Smit, J., H. Engelhardt, …, W. Baumeister. 1992. The S-layer of *Caulobacter crescentus*: three-dimensional image reconstruction and structure analysis by electron microscopy. *J. Bacteriol.* 174:6527–6538.
12. Bingle, W. H., S. G. Walker, and J. Smit. 1993. Definition of form and function for the S-layer of Caulobacter crescentus. *In* Advances in Bacterial Paracrystalline Surface Layers. Springer, Boston, MA, pp. 181–192.
13. Awram, P., and J. Smit. 1998. The *Caulobacter crescentus* paracrystalline S-layer protein is secreted by an ABC transporter (type I) secretion apparatus. *J. Bacteriol.* 180:3062–3069.
14. Toporowski, M. C., J. F. Nomellini, …, J. Smit. 2004. Two outer membrane proteins are required for maximal type I secretion of the *Caulobacter crescentus* S-layer protein. *J. Bacteriol.* 186:8000–8009.
15. Bingle, W. H., J. F. Nomellini, and J. Smit. 2000. Secretion of the *Caulobacter crescentus* S-layer protein: further localization of the C-terminal secretion signal and its use for secretion of recombinant proteins. *J. Bacteriol.* 182:3298–3301.
16. Chenal, A., J. I. Guijarro, …, D. Ladant. 2009. RTX calcium binding motifs are intrinsically disordered in the absence of calcium: implication for protein secretion. *J. Biol. Chem.* 284:1781–1789.
17. Nomellini, J. F., S. Kupcu, …, J. Smit. 1997. Factors controlling in vitro recrystallization of the *Caulobacter crescentus* paracrystalline S-layer. *J. Bacteriol.* 179:6349–6354.
18. Ford, M. J., J. F. Nomellini, and J. Smit. 2007. S-layer anchoring and localization of an S-layer-associated protease in *Caulobacter crescentus*. *J. Bacteriol.* 189:2226–2237.
19. Bingle, W. H., J. F. Nomellini, and J. Smit. 1997. Linker mutagenesis of the *Caulobacter crescentus* S-layer protein: toward a definition of an N-terminal anchoring region and a C-terminal secretion signal and the potential for heterologous protein secretion. *J. Bacteriol.* 179:601–611.
20. Walker, S. G., D. N. Karunaratne, …, J. Smit. 1994. Characterization of mutants of *Caulobacter crescentus* defective in surface attachment of the paracrystalline surface layer. *J. Bacteriol.* 176:6312–6323.
21. Jones, M. D., E. Vinogradov, …, J. Smit. 2015. The core and O-polysaccharide structure of the *Caulobacter crescentus* lipopolysaccharide. *Carbohydr. Res.* 402:111–117.
22. Awram, P., and J. Smit. 2001. Identification of lipopolysaccharide O antigen synthesis genes required for attachment of the S-layer of *Caulobacter crescentus*. *Microbiology.* 147:1451–1460.
23. Poindexter, J. S. 1984. The role of calcium in stalk development and in phosphate acquisition in *Caulobacter crescentus*. *Arch. Microbiol.* 138:140–152.
24. Domínguez, D. C., M. Guragain, and M. Patrauchan. 2015. Calcium binding proteins and calcium signaling in prokaryotes. *Cell Calcium.* 57:151–165.
25. Harris, L. K., N. A. Dye, and J. A. Theriot. 2014. A *Caulobacter* MreB mutant with irregular cell shape exhibits compensatory widening to maintain a preferred surface area to volume ratio. *Mol. Microbiol.* 94:988–1005.
26. Michiels, J., C. Xi, …, J. Vanderleyden. 2002. The functions of Ca^{2+} in bacteria: a role for EF-hand proteins? *Trends Microbiol.* 10:87–93.
27. Benz, R., M. D. Jones, …, J. Smit. 2015. OmpW of *Caulobacter crescentus* functions as an outer membrane channel for cations. *PLoS One.* 10:e0143557.
28. Jobby, M. K., and Y. Sharma. 2007. Caulollins from *Caulobacter crescentus*, a pair of partially unstructured proteins of $\beta\gamma$-crystallin superfamily, gain structure upon binding calcium. *Biochemistry.* 46:12298–12307.
29. Nikolaidis, I., T. Izoré, …, A. Dessen. 2012. Calcium-dependent complex formation between PBP2 and lytic transglycosylase SltB1 of *Pseudomonas aeruginosa*. *Microb. Drug Resist.* 18:298–305.
30. Baranova, E., R. Fronzes, …, H. Remaut. 2012. SbsB structure and lattice reconstruction unveil Ca^{2+} triggered S-layer assembly. *Nature.* 487:119–122.
31. Arbing, M. A., S. Chan, …, R. P. Gunsalus. 2012. Structure of the surface layer of the methanogenic archaean *Methanosarcina acetivorans*. *Proc. Natl. Acad. Sci. USA.* 109:11812–11817.
32. Sára, M., and U. B. Sleytr. 1987. Molecular sieving through S layers of *Bacillus stearothermophilus* strains. *J. Bacteriol.* 169:4092–4098.
33. Koval, S. F., S. H. Hynes, …, E. Jurkevitch. 2013. *Bdellovibrio exovorus* sp. nov., a novel predator of *Caulobacter crescentus*. *Int. J. Syst. Evol. Microbiol.* 63:146–151.
34. de la Fuente-Núñez, C., J. Mertens, …, R. E. W. Hancock. 2012. The bacterial surface layer provides protection against antimicrobial peptides. *Appl. Environ. Microbiol.* 78:5452–5456.
35. Koval, S. F., and S. H. Hynes. 1991. Effect of paracrystalline protein surface layers on predation by *Bdellovibrio bacteriovorus*. *J. Bacteriol.* 173:2244–2249.
36. Asadi, N., N. Chand, and M. Rassa. 2015. Crystalline bacterial surface layer (S-layer) opens golden opportunities for nanobiotechnology in textiles. *IEEE Trans. Nanobioscience.* 14:952–959.
37. Ucisik, M. H., U. B. Sleytr, and B. Schuster. 2015. Emulsomes meet S-layer proteins: an emerging targeted drug delivery system. *Curr. Pharm. Biotechnol.* 16:392–405.
38. Toporowski, M. C., J. F. Nomellini, …, J. Smit. 2005. Transcriptional regulation of the S-layer protein type I secretion system is *Caulobacter crescentus*. *FEMS Microbiol. Lett.* 251:29–36.
39. Walker, S. G., S. H. Smith, and J. Smit. 1992. Isolation and comparison of the paracrystalline surface layer proteins of freshwater *Caulobacters*. *J. Bacteriol.* 174:1783–1792.

40. Smolsky, I. L., P. Liu, …, H. Tsuruta. 2007. Biological small-angle x-ray scattering facility at the Stanford Synchrotron Radiation Laboratory. *J. Appl. Cryst.* 40:s453–s458.

41. Amat, F., F. Moussavi, …, M. Horowitz. 2008. Markov random field based automatic image alignment for electron tomography. *J. Struct. Biol.* 161:260–275.

42. Amat, F., L. R. Comolli, …, M. Horowitz. 2010. Analysis of the intact surface layer of *Caulobacter crescentus* by cryo-electron tomography. *J. Bacteriol.* 192:5855–5865.

43. Smit, J., and N. Agabian. 1982. Cell surface patterning and morphogenesis: biogenesis of a periodic surface array during *Caulobacter* development. *J. Cell Biol.* 95:41–49.

44. Pum, D., and U. B. Sleytr. 2014. Reassembly of S-layer proteins. *Nanotechnology.* 25:312001.

45. Koval, S. F. 1993. Predation on bacteria possessing S-layers. *In* Advances in Bacterial Paracrystalline Surface Layers. Springer, pp. 85–92. http://www.springer.com/us/book/9780306445828.

46. Chung, S., S.-H. Shin, …, J. J. De Yoreo. 2010. Self-catalyzed growth of S-layers via an amorphous-to-crystalline transition limited by folding kinetics. *Proc. Natl. Acad. Sci. USA.* 107:16536–16541.

47. Rad, B., T. K. Haxton, …, C. M. Ajo-Franklin. 2015. Ion-specific control of the self-assembly dynamics of a nanostructured protein lattice. *ACS Nano.* 9:180–190.

48. Kist, M. L., and R. G. E. Murray. 1984. Components of the regular surface array of *Aquaspirillum serpens* MW5 and their assembly in vitro. *J. Bacteriol.* 157:599–606.

49. Beveridge, T. J., and R. G. Murray. 1976. Dependence of the superficial layers of *Spirillum putridiconchylium* on Ca^{2+} or Sr^{2+}. *Can. J. Microbiol.* 22:1233–1244.

50. Doran, J. L., W. H. Bingle, and W. J. Page. 1987. Role of calcium in assembly of the *Azotobacter vinelandii* surface array. *J. Gen. Microbiol.* 133:339–413.

51. Sára, M., B. Kuen, …, U. B. Sleytr. 1996. Dynamics in oxygen-induced changes in S-layer protein synthesis from *Bacillus stearothermophilus* PV72 and the S-layer-deficient variant T5 in continuous culture and studies of the cell wall composition. *J. Bacteriol.* 178:2108–2117.

52. Sotomayor-Pérez, A.-C., D. Ladant, and A. Chenal. 2014. Disorder-to-order transition in the CyaA toxin RTX domain: implications for toxin secretion. *Toxins (Basel).* 7:1–20.

53. O'Brien, D. P., B. Hernandez, …, A. Chenal. 2015. Structural models of intrinsically disordered and calcium-bound folded states of a protein adapted for secretion. *Sci. Rep.* 5:14223.

54. Jones, M. D., A. C. K. Chan, …, J. Smit. 2016. Surface-layer protein from *Caulobacter crescentus*: expression, purification and x-ray crystallographic analysis. *Acta Crystallogr. Sect. F Struct. Biol. Commun.* 72:677–680.

55. Zhu, C., G. Guo, …, M. Sun. 2017. Diversity in S-layers. *Prog. Biophys. Mol. Biol.* 123:1–15.

56. Kirk, J. A., O. Banerji, and R. P. Fagan. 2017. Characteristics of the *Clostridium difficile* cell envelope and its importance in therapeutics. *Microb. Biotechnol.* 10:76–90.

57. Kern, J., and O. Schneewind. 2010. BslA, the S-layer adhesin of *B. anthracis*, is a virulence factor for anthrax pathogenesis. *Mol. Microbiol.* 75:324–332.

58. Poppinga, L., B. Janesch, …, E. Genersch. 2012. Identification and functional analysis of the S-layer protein SplA of *Paenibacillus larvae*, the causative agent of American foulbrood of honey bees. *PLoS Pathog.* 8:e1002716.

59. Garduño, R. A., A. R. Moore, …, W. W. Kay. 2000. Host cell invasion and intracellular residence by *Aeromonas salmonicida*: role of the S-layer. *Can. J. Microbiol.* 46:660–668.

60. Al-Karadaghi, S., D. N. Wang, and S. Hovmöller. 1988. Three-dimensional structure of the crystalline surface layer from *Aeromonas hydrophila*. *J. Ultrastruct. Mol. Struct. Res.* 101:92–97.

61. Bingle, W. H., J. F. Nomellini, and J. Smit. 1997. Cell-surface display of a *Pseudomonas aeruginosa* strain K pilin peptide within the paracrystalline S-layer of *Caulobacter crescentus*. *Mol. Microbiol.* 26:277–288.